Korean J. Chem. Eng., **28**(3), 686-696 (2011)
DOI: 10.1007/s11814-010-0407-0

Experiment and 3D simulation of slugging regime in a circulating fluidized bed

Cholthicha Amornsirirat, Benjapon Chalermsinsuwan, Lursuang Mekasut, Prapan Kuchonthara, and Pornpote Piumsomboon†

Center for Petroleum, Petrochemicals and Advanced Materials,
Chulalongkorn University, Phayathai Road, Patumwan, Bangkok 10330, Thailand
(*Received 25 May 2010 • accepted 20 August 2010*)

Abstract−A circulating fluidized bed (CFB) is widely applied in many industries because it has high efficiency. To develop and improve the process, an understanding of the hydrodynamics inside the CFB is very important. Computational fluid dynamics (CFD) represents a powerful tool for helping to understand the phenomena involved in the process. In this study, a CFD model was developed to represent a cold model of the laboratory scale CFB which was designed to study the hydrodynamics of a CFB using commercial CFD software. The Eulerian approach with kinetic theory of granular flow was used for simulating the hydrodynamics inside the system. After proper tuning of relevant parameters, the pressure profile along the equipment from the simulation was well agreed with that from the experiment. The simulation result expresses the hydrodynamic parameters of the slug flow such as solid volume fraction, gas and solid velocities and granular temperature in the riser.

Key words: Computational Fluid Dynamics, Circulating Fluidized Bed, Slug Flow, Eulerian Approach, Kinetic Theory of Granular Flow

INTRODUCTION

A circulating fluidized bed (CFB) is widely employed in many industries, including coal combustion for large-scale thermal power generation and catalytic cracking of petroleum to produce gasoline and other fuels. In most cases, the scale-up to large commercial applications involves a costly stepwise process of building and testing several sizes of pilot-scale and cold model operations [1]. Frequently, the final design can take months or years to reach full production capacity. The main reason for these design problems is the flow behavior inside a circulating fluidized bed and its specific operating conditions [1,2]. Moreover, the fluidizability of the particles is also a major consideration. Typically, sand is used as bed material; however, alumina (Al_2O_3) ball particles are also used as an alternative. The average size of the alumina particles is about 2-3 mm and particle densities 3,950-4,100 kg/m^3. It is categorized as Geldart group D particle [3]. This type of particle, is difficult to fluidize and tends to behave erratically. A large amount of gas therefore is needed. The fluidization with Geldart D particles leads to bubble coalescence and creates large bubbles. When the bubble size is growing close to the bed diameter, the bed is separated into slices of emulsion. The particles flow past the bubble in an annular region on the wall or rain through the bubble. Then the slug flow can be observed [4]. The mechanism for the slug flow is of great importance to be understood. In the past, a few efforts, mainly experimental, have been made, leading to various empirical formulations for determining macroscopic slugging phenomena [5-7]. However, better quantitative understanding of the hydrodynamics is highly required for design and scale-up of efficient circulating fluidized bed reactors.

†To whom correspondence should be addressed.
E-mail: pornpote.p@chula.ac.th

Computational fluid dynamics (CFD) is a powerful tool that can provide better understanding of hydrodynamics inside the flow domain for both single-phase and multi-phase flows. Typically, the Eulerian approach is used to model multiphase gas-solid fluidized beds. There are two constitutive models for the Eulerian approach: the viscosity model and the kinetic theory of granular flows (KTGF) model [8]. The kinetic theory of granular flow has found the widest use as a constitutive model. This theory is basically an extension of the classical kinetic theory of gases to dense gas-solid flows, with a description of the solid particle collisions by means of the restitution coefficients. In this study, commercial CFD software was used to model the flow phenomena inside the experimental CFB in our laboratory in order to explain the hydrodynamics inside the riser and relate the results with the hydrodynamic parameters such as solid volume fraction, gas and solid velocities and granular temperature.

EXPERIMENTAL

Fig. 1 shows the actual and schematic CFB experimental apparatus. The apparatus consisted of an acrylic cylindrical riser, a cyclone, a downcomer, and return leg connecting with each other. The cylindrical riser was 0.0334 m. in diameter and 3.375 m in height. The cyclone dimension was constructed with a height of 0.32 m and a maximum diameter of 0.092 m. The diameters of the downcomer and the return leg were 0.101 m and 0.0334 m, respectively. To monitor the pressure profile inside the experimental unit, differential pressure transmitters were installed and the measurement was conducted along the system shown as P1-P8 in Fig. 1. The bed material was alumina (Al_2O_3) particles with a diameter of 2 mm and density of 3,970 kg/m^3. The gas entered the bottom of the riser with a velocity of 4.76 m/s. The bed material flowed upward to the cyclone, separated and returned to the downcomer. The hydrodynamics inside

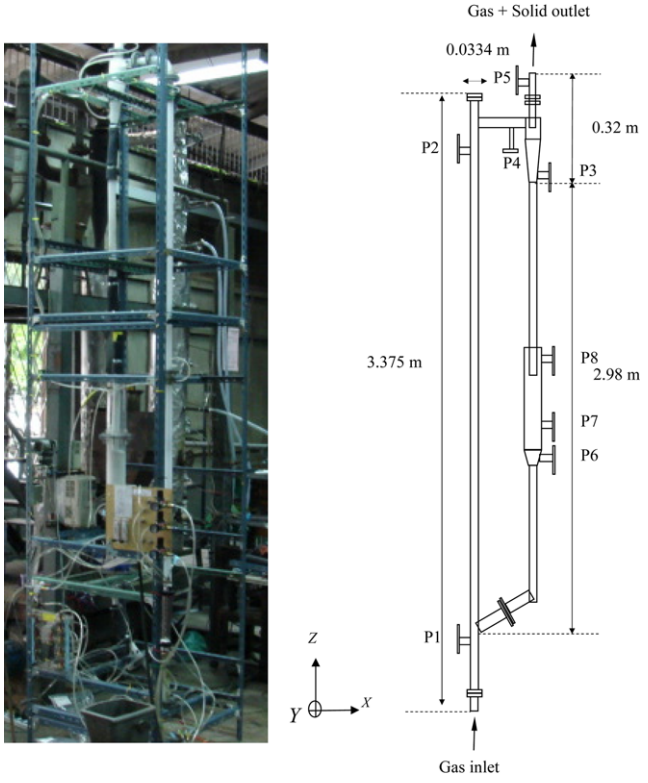

Fig. 1. A circulating fluidized bed (CFB) and schematic drawing of CFB.

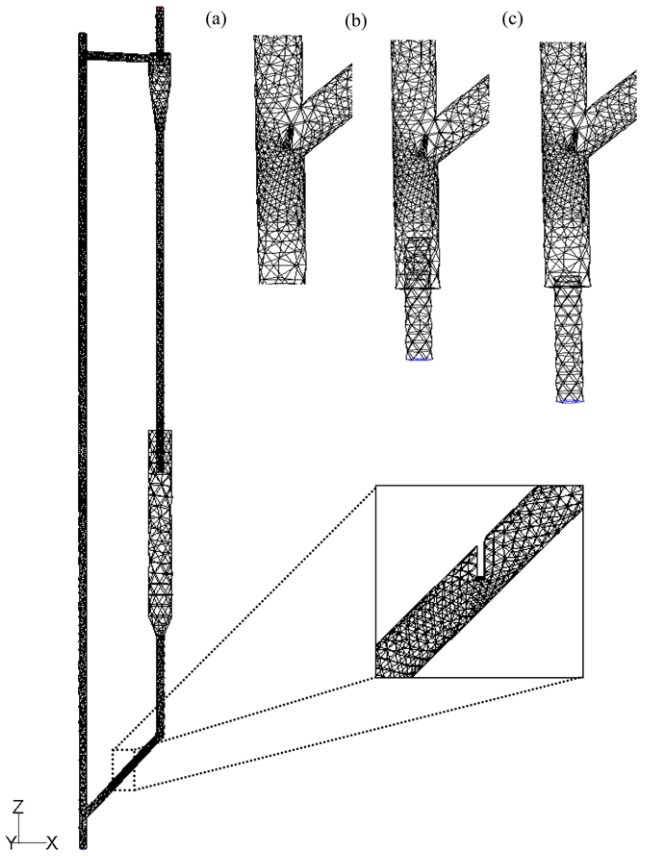

Fig. 2. Computational domain of the CFB with (a) no feed injection, (b) 5 cm tube feed injection and (c) 2 cm tube feed injection.

the experimental CFB was observed via the pressure measurement along the riser. The data was collected and compared with the simulation results described in the next section.

COMPUTATIONAL FLUID DYNAMICS SIMULATION

1. Mathematical Model

A CFB model was developed to represent the laboratory-scale CFB apparatus as shown in Fig. 2 with its computational domain. Then, its computational domain information was exported to the CFD program to define the physical space for the simulation. A commercial CFD program, FLUENT 6.2.16, was used for modeling the system. To describe the hydrodynamics inside the riser, a set of mass and momentum conservation equations for both gas and solid phases was numerically solved together with the constitutive equations. There are several models for gas-solid flow system such as the Eulerian and Lagrangian models [8]. In this study, the Eulerian

Table 1. A summary of the governing equations and constitutive equations

A. Governing equations:

(1) Conservation of mass:

(a) Gas phase:

$$\frac{\partial}{\partial t}(\varepsilon_g \rho_g) + \nabla \cdot (\varepsilon_g \rho_g \mathrm{v}_g) = 0 \quad (1)$$

(b) Solid phase:

$$\frac{\partial}{\partial t}(\varepsilon_s \rho_s) + \nabla \cdot (\varepsilon_s \rho_s \mathrm{v}_s) = 0 \quad (2)$$

(2) Conservation of momentum:

(a) Gas phase:

$$\frac{\partial}{\partial t}(\varepsilon_g \rho_g \mathrm{v}_g) + \nabla \cdot (\varepsilon_g \rho_g \mathrm{v}_g \mathrm{v}_g) = -\varepsilon_g \nabla \mathrm{P} + \nabla \cdot \tau_g + \varepsilon_g \rho_g \mathrm{g} - \beta_{gs}(\mathrm{v}_g - \mathrm{v}_s) \quad (3)$$

(b) Solid phase:

$$\frac{\partial}{\partial t}(\varepsilon_s \rho_s \mathrm{v}_s) + \nabla \cdot (\varepsilon_s \rho_s \mathrm{v}_s \mathrm{v}_s) = -\varepsilon_s \nabla \mathrm{P} + \nabla \cdot \tau_s - \nabla \mathrm{P}_s + \varepsilon_s \rho_s \mathrm{g} + \beta_{gs}(\mathrm{v}_g - \mathrm{v}_s) \quad (4)$$

Table 1. Continued

(3) Conservation of solid phase fluctuating energy:

$$\frac{3}{2}\left[\frac{\partial}{\partial t}(\varepsilon_s\rho_s\theta)+\nabla\cdot(\varepsilon_s\rho_s\theta)\mathrm{v}_s\right]=(-\nabla \mathrm{p}_s\bar{\mathrm{I}}+\tau_s):\nabla\mathrm{v}_s+\nabla\cdot(\mathrm{k}_s\nabla\theta)-\gamma_s+\phi_s \quad (5)$$

B. Constitutive equations:

(a) Gas phase stress:

$$\tau_g=\varepsilon_g\mu_g[\nabla\mathrm{v}_s+(\nabla\mathrm{v}_g)^T]-\frac{2}{3}\varepsilon_g\mu_g(\nabla\cdot\mathrm{v}_g)\mathrm{I} \quad (6)$$

(b) Solid phase stress:

$$\tau_s=\varepsilon_s\mu_s[\nabla\mathrm{v}_s+(\nabla\mathrm{v}_s)^T]-\varepsilon_s\left(\xi_s-\frac{2}{3}\mu_g\right)\nabla\cdot\mathrm{v}_g\mathrm{I} \quad (7)$$

(c) Collisional dissipation of solid fluctuating energy:

$$\gamma_s=3(1-\mathrm{e}^2)\varepsilon_s^2\rho_s\mathrm{g}_0\theta\left(\frac{4}{\mathrm{d}}\sqrt{\frac{\theta}{\pi}}\right) \quad (8)$$

(d) Radial distribution function:

$$\mathrm{g}_0=\left[1-\left(\frac{\varepsilon_s}{\varepsilon_{s,max}}\right)^{1/3}\right]^{-1} \quad (9)$$

(e) Solid phase pressure:

$$\mathrm{p}_s=\varepsilon_s\rho_s\theta[1+2\mathrm{g}_0\varepsilon_s(1+\mathrm{e})] \quad (10)$$

(f) Solid phase shear viscosity:

$$\mu_s=\frac{4}{5}\varepsilon_s^2\rho_s\mathrm{d}\mathrm{g}_0(1+\mathrm{e})\sqrt{\frac{\theta}{\pi}}+\frac{10\rho_s\mathrm{d}\sqrt{\pi\theta}}{96(1+\mathrm{e})\mathrm{g}_0\varepsilon_s}\left[1+\frac{4}{5}\mathrm{g}_0\varepsilon_s(1+\mathrm{e})\right]^2 \quad (11)$$

(g) Solid phase bulk viscosity:

$$\xi_s=\frac{4}{5}\varepsilon_s^2\rho_s\mathrm{d}\mathrm{g}_0(1+\mathrm{e})\sqrt{\frac{\theta}{\pi}} \quad (12)$$

(h) Exchange of the fluctuating energy between gas and solid:

$$\phi_s=-3\beta_{gs}\theta \quad (13)$$

(i) Gas-solid phase interphase exchange coefficient:

Wen-Yu model:

$$\beta_{gs}=\frac{3}{4}\mathrm{C}_D\frac{\varepsilon_s\varepsilon_g\rho_g|\mathrm{v}_g-\mathrm{v}_s|}{\mathrm{d}}\varepsilon_g^{-2.65} \quad (14)$$

with

$$\mathrm{C}_D=\frac{24}{\mathrm{Re}_k}(1+0.15\mathrm{Re}_k^{0.687});\quad \mathrm{Re}_k=\frac{\rho_g\varepsilon_g|\mathrm{v}_g-\mathrm{v}_s|\mathrm{d}}{\mu_g}$$

Gidaspow model:

when $\varepsilon_g>0.80$:

$$\beta_{gs}=150\frac{(1-\varepsilon_g)^2\mu_g}{\varepsilon_g\mathrm{d}^2}+1.75\frac{(1-\varepsilon_g)\rho_g|\mathrm{v}_g-\mathrm{v}_s|}{\mathrm{d}} \quad (15)$$

when $\varepsilon_g\le 0.80$:

$$\beta_{gs}=\frac{3(1-\varepsilon_g)\varepsilon_g}{4\mathrm{d}}\rho_g|\mathrm{v}_g-\mathrm{v}_s|\mathrm{C}_{D0}\varepsilon_g^{-2.65} \quad (16)$$

with

$$\mathrm{Re}<1000:\ \mathrm{C}_{D0}=\frac{24}{\mathrm{Re}_k}(1+0.15\mathrm{Re}_k^{0.687});\quad \mathrm{Re}_k=\frac{\rho_g\varepsilon_g|\mathrm{v}_g-\mathrm{v}_s|\mathrm{d}}{\mu_g}$$

$$\mathrm{Re}\ge 1000:\ \mathrm{C}_{D0}=0.44$$

model was selected since the disperse phase has high volume fraction. The kinetic theory of granular flow, representing the conservation of solid fluctuation energy, was used for closure of the solids' property terms. Wen and Yu and Gidaspow drag models [9] were used to model the momentum exchange between phases by calculating the interphase exchange coefficients. The governing equations and constitutive equations [10-14] for these models are given in Table 1.

2. Initial and Boundary Conditions

Fig. 3 shows the model description, mode of operation, system parameters, including initial and boundary conditions for both phases. The bed material in the system was alumina (Al_2O_3) particles and the transport medium was air. Initially, the particles were packed in the downcomer with the solid volume fraction of 0.54 at the height of 2 m from the bottom of downcomer. The air was supplied from the bottom of the riser with the velocity of 4.76 m/s and the pres-

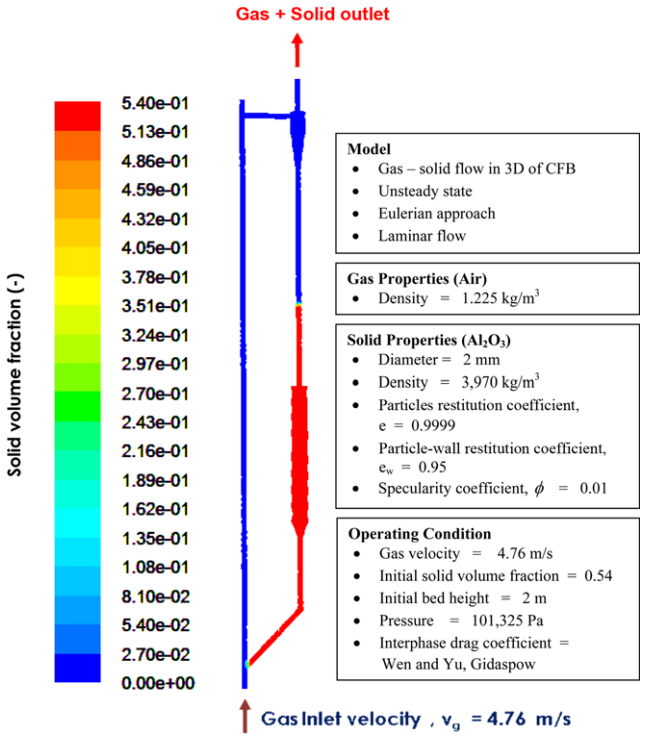

Fig. 3. Model description with initial and boundary conditions used in the simulations of the CFB.

sure at the outlet was specified as atmospheric pressure. At the wall, a no-slip condition was applied for all velocities, except for the tangential velocity of the solid phase and the granular temperature. Here, the boundary conditions of Johnson and Jackson were used instead [15].

RESULTS AND DISCUSSION

The experimental CFB apparatus was run with the same condition described in the previous section. After the system reached quasi-steady state condition, the pressures inside the riser were recorded and the pressure profile was plotted as shown in Fig. 4. It was observed that the pressure at P1 position was the highest and decreased along the riser from P1 position to P2 position. Then the pressure decreased further from P2 to P5 position where the port opened to the atmosphere and started to increase when the flow passed through the cyclone due to the accumulation of falling particles. After that, the pressure increased along the downcomer. The pressure slightly decreased when the flow passed through the chamber in the middle of the downcomer and the pressure in the loop increased again and eventually returned to the value of the inlet pressure.

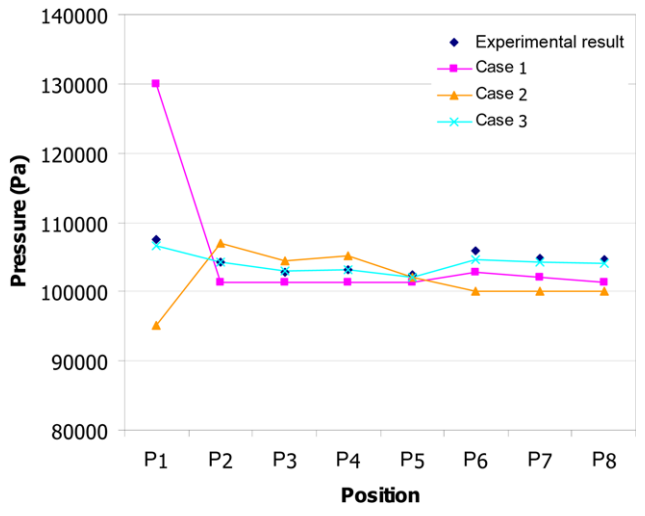

Fig. 4. Pressure profiles of the three cases: Case 1; no feed injection, Case 2; 5 cm tube feed injection and Case 3; 2 cm tube feed injection, comparing the experimental results.

1. Comparison of the Experimental and Simulation Results

The CFD model as described in the previous section was developed and simulated. The results were plotted along with the experimental result as shown in Fig. 4. One can observe that most of the pressure estimation along the circulating loop was close to the experimental data. However, there is a point of great discrepancy between the experimental and the simulation results: the pressure at the P1 position. In the actual apparatus there is a gas probe installed on the distributor plate. However, the exact length was not measured due to the limitation of the apparatus accessment. Thus, the CFD model was modified in order to obtain the same pressure profile as the experiment. Figs. 2(b) and (c) show the modification where the feed injection probes were introduced with the height of 5 cm and 2 cm from the distributor plate, respectively. The pressure profiles from the simulation results with these modifications are labeled as Case 2, and Case 3 in Fig. 4. It was found that the Case 3 simulation produced the result that most coincided with the experimental data for all the points along the CFB loop, especially the P1 position. Although most of the points along the pressure profile in the Case 2 simulation were close to the experimental data, the pressure at the P1 position was still much lower than the experimental result. Thus, the Case 3 simulation result will be used for further analysis in the next section.

Before using the simulation results for further analysis, it is required to confirm that the simulation results were independent of grid size. Thus, increments of grid numbers in the simulation domain were performed. Three grid sizes for the computational domains, which are 20,116, 29,088 and 48,092 cells, were employed for validation. Fig. 5 shows the pressure profiles with three grid sizes when com-

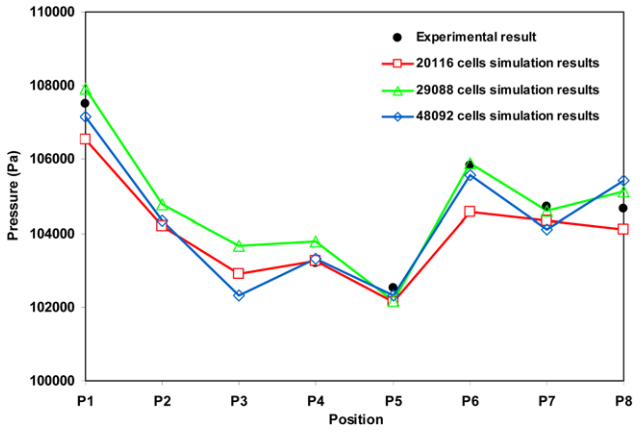

Fig. 5. Pressure profiles of the three-gird size difference (a) 20,116 cells, (b) 29,088 cells and (c) 48,092 cells.

paring to experimental data. From the figures, all the grid number increment gave the same accuracy of prediction. Therefore, in order to save the computation time, the computational domain with 20,116 cells was selected for the analysis. Fig. 6 shows various time-averaged pressure profiles from 40-50 seconds to 40-80 seconds. All time-averaged pressure profiles give a similar prediction. Therefore, it can be concluded that the time-averaged pressure profiles obtained from any average values in this study are the representatives of the pressure profiles along the system.

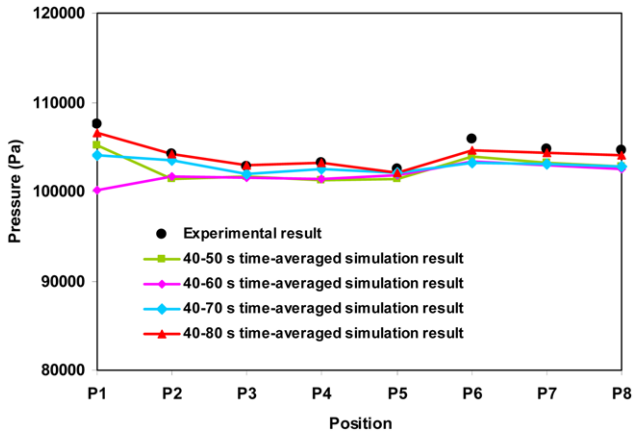

Fig. 6. The time-averaged pressure profile of grid sizes 20,116 cells simulation results along the position of CFB.

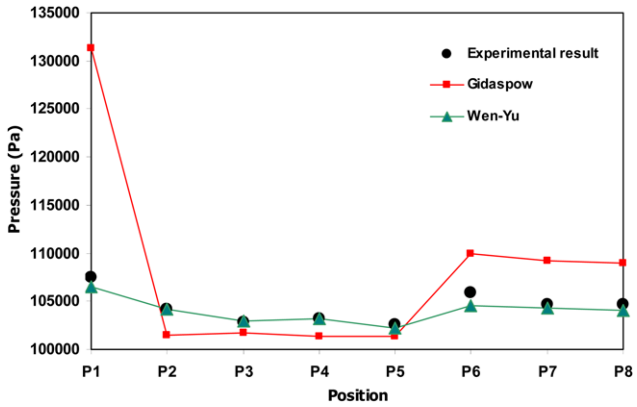

Fig. 7. Pressure profiles along the CFB loop when using Gidaspow and Wen-Yu drag model compared with the experimental result.

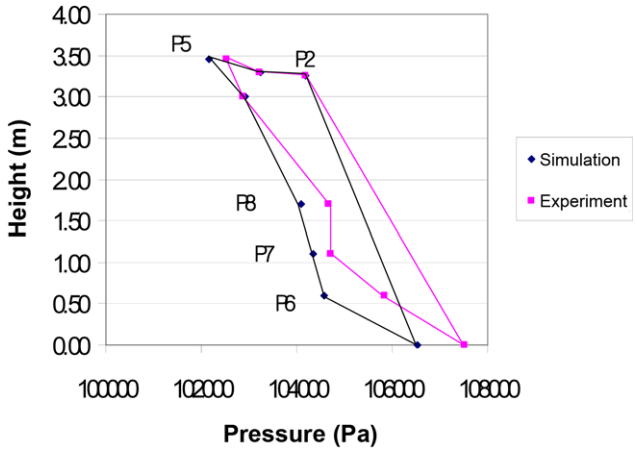

Fig. 8. Pressure loops inside the CFB apparatus at each of positions, comparing the experimental result with Case 3 simulation result.

2. Effect of Drag Model

Two drag coefficient models available in FLUENT, Gidaspow and Wen and Yu models [9] were selected to simulate the hydrodynamics inside the CFB. Fig. 7 shows the comparison of the pressure profiles generated by using these drag coefficients. It was found that the pressure profiles by the Wen and Yu drag model provides better estimation than those by Gidaspow model, especially the pres-

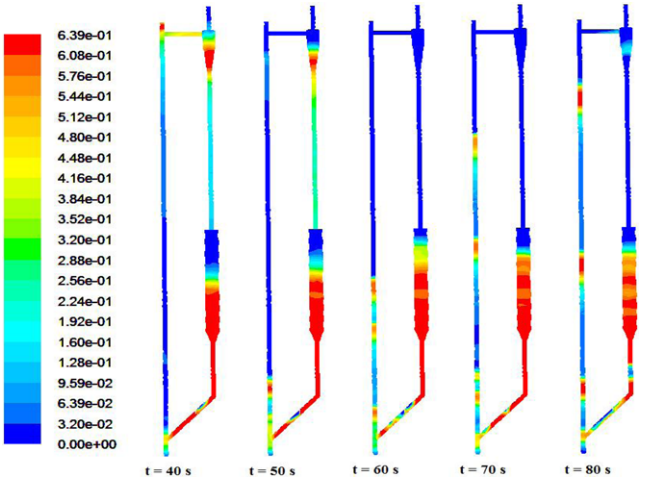

Fig. 9. a. Transient distribution of Al_2O_3 solid volume fraction inside the circulating fluidized bed system.

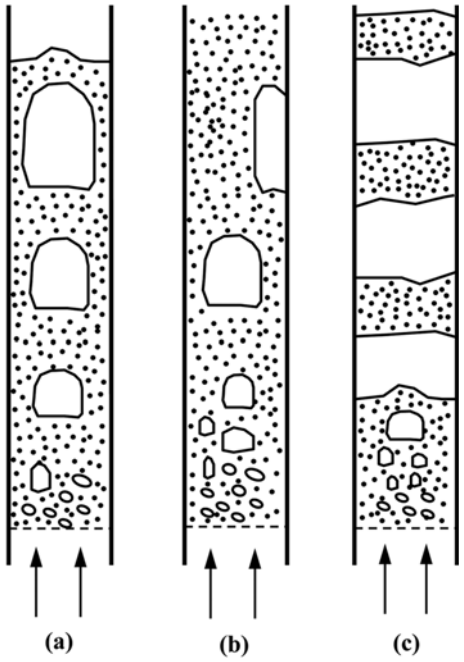

Fig. 9. b. Type of slugs formed in fluidized beds: (a) axial slugs - fine smooth particles; (b) wall slugs - fine rough particles, rough walls, high velocity; (c) flat slugs - large particles (Geldart D) [19,20].

sure at P1 position. The pressure predictions at P1, P6, P7 and P8 provided by Gidaspow model were higher than the experimental results. The reason was that Gidaspow model was developed for a dense system [9,16,17]. The prediction values by Gidaspow thus were overshot. In fact, the particle densities at those positions were lighter than those in other parts. The Wen and Yu model is more suitable for the prediction of the dilute system [9]. Therefore, it was chosen to simulate the hydrodynamics inside the CFB in this study.

Fig. 8 shows the pressure loops along the CFB apparatus obtained from both experimental and simulation results. The pressure loop gives the pressure allocation at different position inside the system. Similar to the Case 3 result in Fig. 4, these pressure loops seem to reasonably fit well with each other. However, when considering only the riser section, the figure shows that the simulation result slightly underestimates the pressure drop along the riser.

3. Hydrodynamics Inside the CFB

3-1. Flow Pattern

To study the hydrodynamics inside the CFB model, the 40-80 s time-averaged values of various parameters such as solid volume fraction, solid velocity and gas velocity were investigated. Fig. 9(a) shows the transient concentration of the solid volume fraction along the CFB system at various instantaneous times. The color represents the solid concentration: red color represents high concentration (0.639) while the blue color represents low concentration (0.0). The figure also shows the segregation of gas and solid phases along the riser.

According to Kunii and Levenspiel [1], the flow patterns in a circulating fluidized bed can be classified into three categories (illustrated in Fig. 9b): (a) axial slugs - fine smooth particles, (b) wall slugs - fine rough particles, rough walls, high velocity and (c) flat slugs - large particles (Geldart D). According to the observation, there is a segregation of gas and solid phases along the riser. Thus the flow in the experiment belongs to the flat slug as shown in Fig. 9c, which coincides with the simulation result shown in Fig. 9a.

Fig. 10(a) shows the solid volume fraction along the height of the riser in the CFB for various time-averaged simulation results. One can observe the solid accumulation at the bottom of the riser where it is the junction between riser and downcomer. The parti-

Fig. 9. c. The snapshots from the CFB experiment in the laboratory demonstrating the slug flow pattern inside the column.

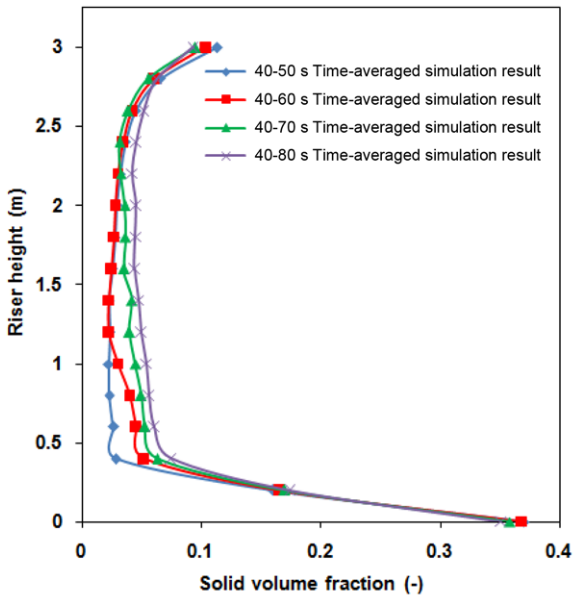

(a)

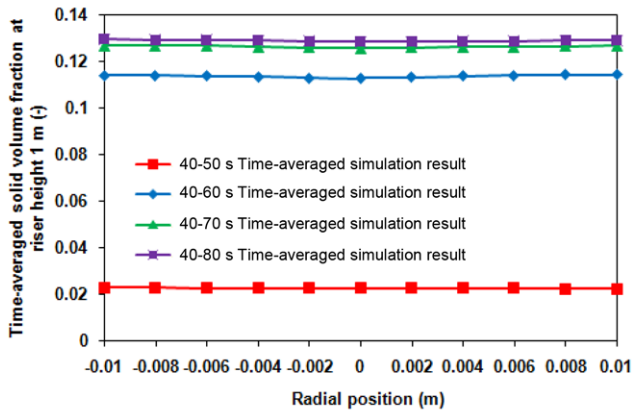

(b)

Fig. 10. (a) The time-averaged axial solid volume fraction along the height in this study. (b) The radial distribution of time-averaged solid volume fraction at 1 m above the bottom of the riser.

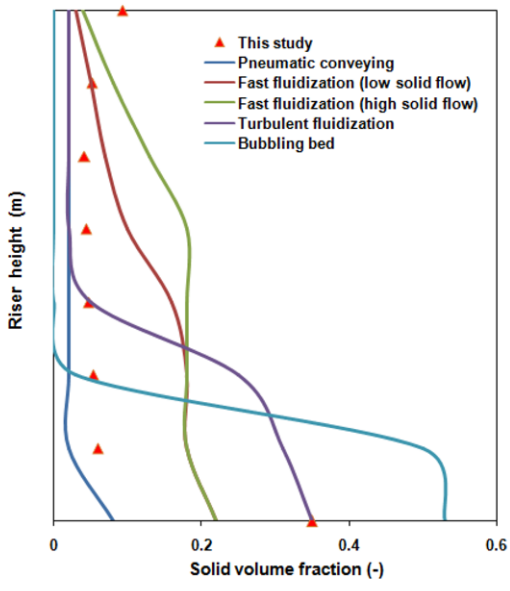

(a)

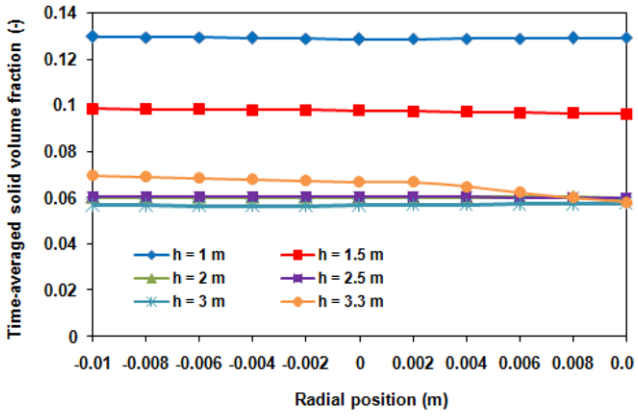

(b)

Fig. 11. (a) The time-averaged axial solid volume fraction along the height, comparing between Kunii and Levenspiel [1] with this study. (b) The radial distribution of time-averaged solid volume fraction at six different heights above the bottom of the riser.

cles from the cyclone fall through the downcomer and return to the riser. The solid volume fraction in this dense phase is approximately 0.35. Then the solid volume fraction was quite uniform along the riser with the value of 0.05. The particle density increases again at the top of the riser where the particles accumulate at the entrance of the connecting pipe with the cyclone. The solid volume fraction at this position was approximately 0.1. On the contrary, the time-averaged solid volume fractions in radial direction at riser height of 1 m above the entrance were quite uniform for the whole range of consideration as shown in Fig. 10(b). The value was about 0.13.

Fig. 11(a) shows the distribution of solid volume fraction along the riser obtained from the simulation compared with those values from Kunii and Levenspiel study [1]. It was observed that the flow pattern from the simulation falls in the range between turbulent and fast fluidization. Typically, in turbulent fluidization the flow is characterized by two different coexisting regions, which are a dense bubbling at the lower region and dilute dispersed flow at the upper region [2]. However, the observation from Fig. 9a was not consistent with the phenomena described above. The observation was that the bed was separated into slices of emulsion by gas media. The phenomenon was not similar to he fast fluidization as well. In fast fluidization, the solid volume fraction is also dense at the bottom, but it is less dense than the turbulent one. Moving up along the riser, the solid volume fraction decreases with the height of the riser. Therefore in this study, the flow pattern falls in the category of the flat slugs flow. Fig. 11(b) shows the time-averaged radial profiles of the solid volume fraction at various height of the riser. The results show the same tendency as observed from Fig. 10(b), except at the height 3.3 m of the riser. The solid volume fraction on the right-end of the riser slightly decreased due to the solids passing to the downcomer.

3-2. Velocity Profiles Along Both Axial and Radial Directions

From the study of the flow pattern inside the CFB, it was found that the flow pattern is in flat slugs flow regime. Then, the gas and

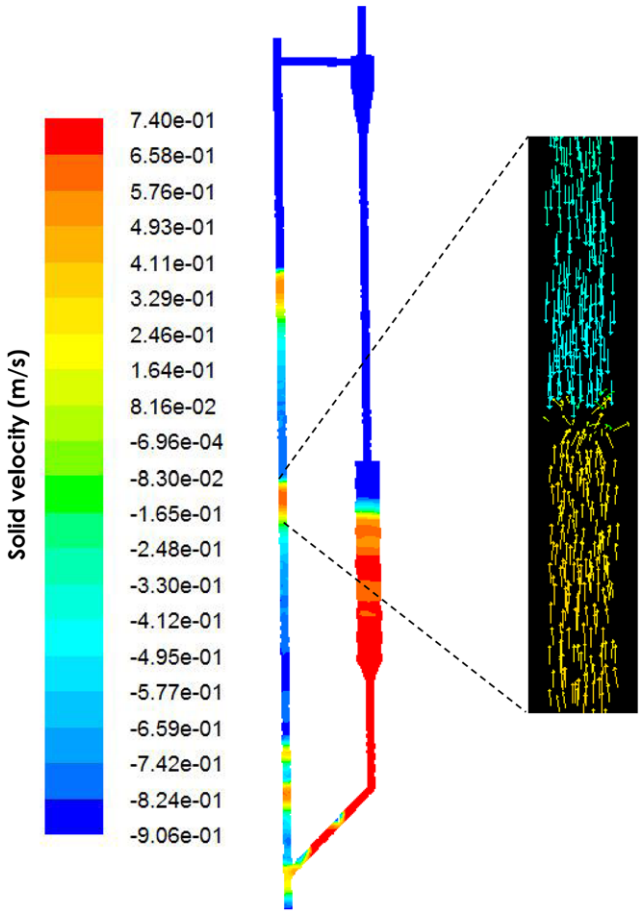

Fig. 12. Contour of solid volume fraction and vector of solid velocity at the 70 seconds time simulation results.

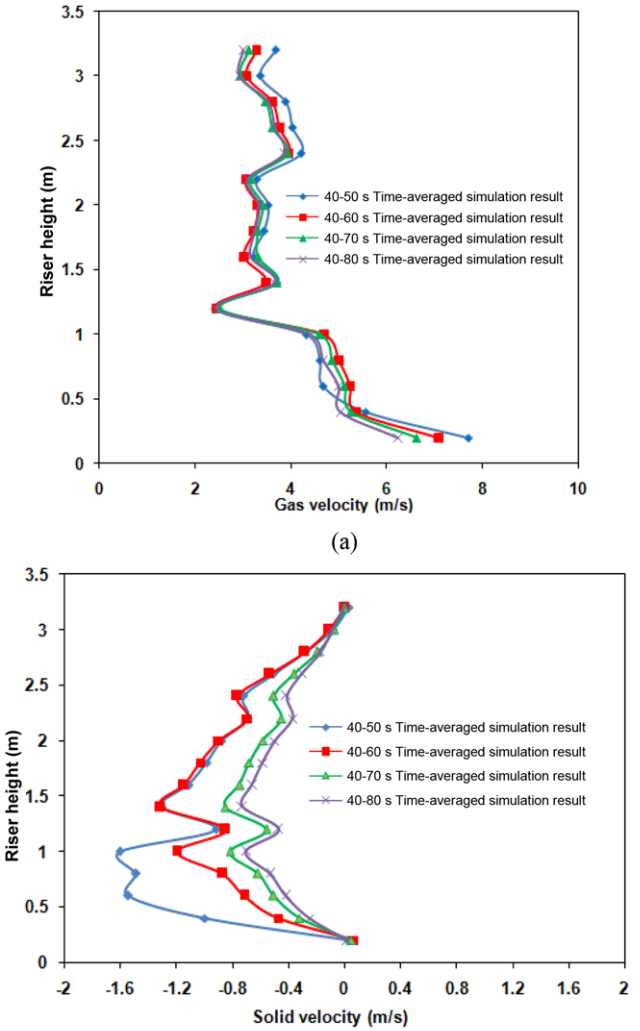

Fig. 13. (a) The time-averaged simulation results of gas velocity along the height of riser in CFB system. (b) The time-averaged simulation results of solid velocity along the height of riser in CFB system.

solid velocity profiles in both axial and radial directions were investigated. Fig. 12 shows the solid volume fraction and vectors of solid velocity from the computation at the 70 seconds time. As one can observe, there are a few slugs moving upward towards the top of the riser as shown by the high values of solid volume fraction. When considering the velocity vectors in the vicinity of the slug, one will find both upward velocity vectors, representing by the yellowish arrows, and the downward velocity vectors, represented by the blue arrows. This implies that the particles flow inside the riser in both directions. However, the particles formulating as a slug are moving upward, while the rest of the particles are moving downward.

Figs. 13(a) and 13(b) show the time-averaged gas velocities and solid velocities along the riser. It was found that the gas velocities above 1 m height of the riser were quite uniform with the average value of 3 m/s. However, the velocities near the bottom region of the riser were much higher than those in the upper region. The average value was around 5 m/s. The reason was that in the upper region the solid concentration was dilute while at the bottom section, the solid population was denser. On the contrary, Fig. 13(b) shows that most of the solid particles are moving downward with the average velocity of −0.3 m/s. Only few particles are moving upward, those being near the upper exit channel.

Figs. 14(a) and 14(b) show the radial distribution of time-averaged gas and solid velocities at a riser height of 1 m. The results show that the time-averaged radial gas velocities are high at the center of the riser and low near the wall, as expected. In case of the solid velocity, the observation was similar, but with opposite direction. The solid velocity is high in the center of the riser and low near the wall in the direction of downward flow since most of the solid particles are moving downward. Therefore, it is consistent with solid velocity vectors shown in Fig. 12. The plots of radial distribution of time-averaged of the gas and solid velocities at six different heights are shown in Figs. 15(a) and 15(b). The patterns of the velocity profiles are similar, except at the top of the riser. At this position, both radial profiles are flat. The reason was that the solid volume fraction was very dilute. The interaction between gas and solid was minimal.

3-3. Granular Temperature

In KTGF model, the granular temperature is one of hydrodynamic parameters which reflects solid fluctuating kinetic energy or oscillation. There are two kinds of granular temperature: classical or particle oscillation and turbulent or bubble oscillation. To compute the granular temperature, the related equations have to be coded into

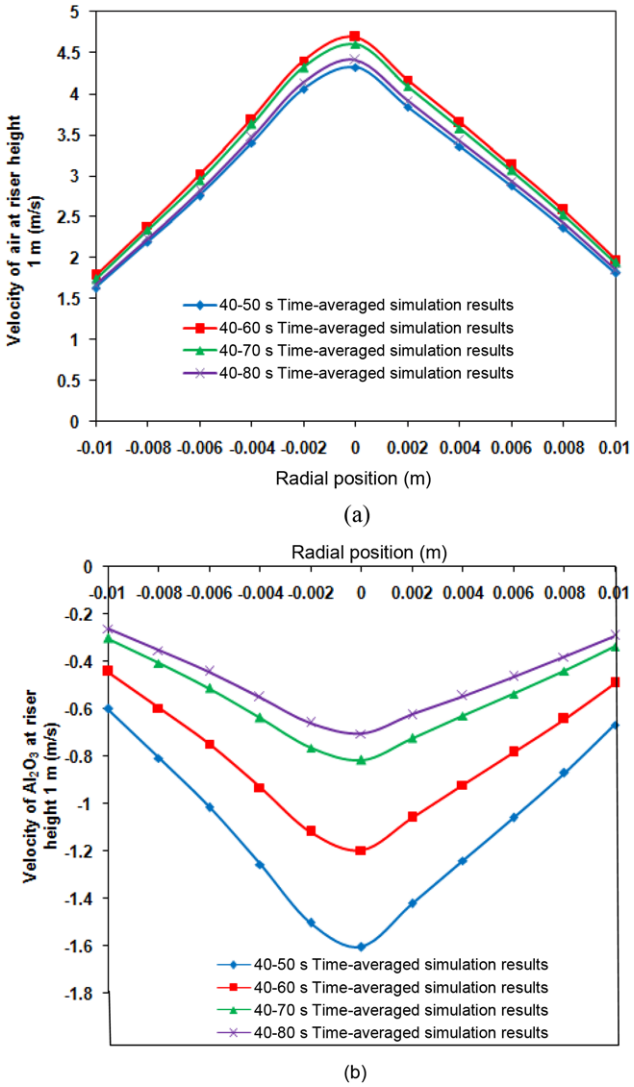

Fig. 14. (a) The radial distribution of time-averaged gas velocity at the riser height of 1 m in CFB system. (b) The radial distribution of time-averaged solid velocity at riser height of 1 m in CFB system.

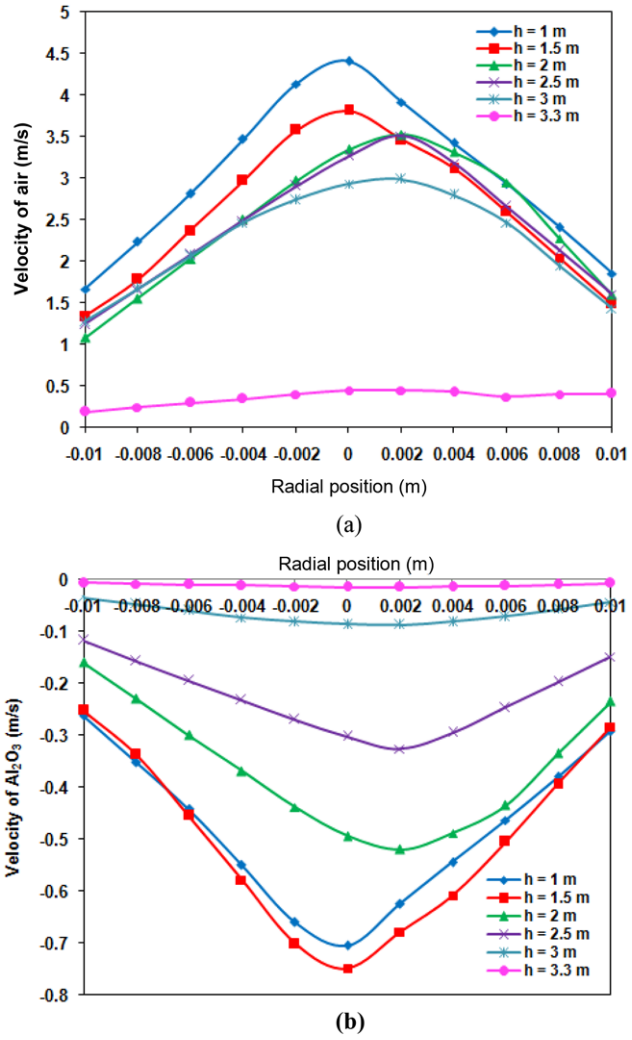

Fig. 15. (a) The radial distribution of time-averaged gas velocity at six different heights (1 m to 3.3 m) above the bottom of the riser. (b) The radial distribution of time-averaged solid velocity at six different heights (1 m to 3.3 m) above the bottom of the riser.

the CFD commercial program. The code itself computes the classical granular temperature (θ), similar to the calculation of single-phase turbulence by direct numerical computation. The turbulent granular temperature (θ_t) is defined as the average of the normal Reynolds stresses ($\overline{v'v'}$), which are the average of the three squares of the fluctuating velocity components in three directions, by using the following definition [18]:

$$\theta_t(t,x) \cong \frac{1}{3}\overline{v_x'v_x'} + \frac{1}{3}\overline{v_y'v_y'} + \frac{1}{3}\overline{v_z'v_z'} \quad (17)$$

The sum of the classical and turbulent granular temperatures is the total granular temperature or the overall solid fluctuating kinetic energy. Table 2 shows the computed time-averaged total granular temperature at six different heights in this CFB system. In general, the granular temperature will be low when the solid volume fraction is very low, since the solid population is lean. Then, the granular temperature will gradually increase as the solid population increases.

Table 2. The computed time-averaged total granular temperature at six different heights in this CFB system

Riser height (m)	Velocity of solid			Total granular temperature
	x	y	z	
0.5	5.9135E-06	3.0750E-06	2.1065E-01	0.1229
1.0	9.0661E-06	7.2451E-06	2.3559E-01	0.1594
1.5	1.8718E-05	2.8926E-06	2.0935E-01	0.1445
2.0	2.1510E-06	5.2581E-07	1.1764E-01	0.0742
2.5	7.1311E-07	1.0169E-06	6.3992E-02	0.0322
3.0	1.3490E-06	1.3494E-06	2.2478E-02	0.0100

After a certain value of solid population, the solid population becomes very dense and the mean free path of the particle movement becomes very short. Subsequently, the granular temperature turns to low value again. In this study the solid is dense near the bottom of the riser and it is very dilute at the top of the riser. The computa-

tional values of granular temperature also demonstrated such a difference with the maximum value of total granular temperature of 0.1594 at the riser height of 1 m and the minimum value of total granular temperature of 0.0100 at the riser height of 3 m. These values belong to the region where the granular temperature is increasing with the increase of the solid volume fraction. Their values also show that in the range of 0 to 1.5 m height of the riser, the solid concentration in the riser was in the same order of magnitude. Beyond 2 m high, the solid concentration in the riser was decreasing and was very light near the top of the riser since its granular temperature was one order of magnitude different between granular temperatures at 1 m and 3 m height.

CONCLUSIONS

A 3D CFD model of a circulating fluidized bed was developed to study the hydrodynamics inside a laboratory CFB apparatus. The model was developed by using the Eulerian-Eulerian approach with the kinetic theory of granular flow. Two drag models were investigated and the Wen and Yu drag model was selected. The results were validated by comparing the simulation results with the obtained pressure profiles and photographs from the experimental results. Then the simulation results were used to describe the hydrodynamic behaviors inside the apparatus. It was found that the solid volume fraction in this dense phase was approximately 0.35, while this was quite uniform along the riser with the value of 0.05. The gas velocities above 1 m height of the riser were uniform with the average value of 3 m/s, while the velocities near the bottom region of the riser were as high as 5 m/s. The granular temperature at the 1 m height was one order of magnitude higher than that at 3 m height, which implied that the overall solid fluctuating kinetic energy at lower region was much higher than the upper region.

ACKNOWLEDGEMENTS

This work was supported by the Fuels Research Center, Department of Chemical Technology, Faculty of Science, Chulalongkorn University, the Center of Excellence for Petroleum, Petrochemicals, and Advanced Materials and Energy Policy and Planning Office (EPPO), Ministry of Energy, Thailand.

NOMENCLATURE

General Letters

C_D : drag coefficient for Wen and Yu model [-]
C_{D0} : drag coefficient for Gidaspow model [-]
d : particle diameter [m]
e : restitution coefficient between particles [-]
e_W : restitution coefficient between particle and wall [-]
g : gravity force [m/s^2]
g_0 : radial distribution function [-]
h : height of riser [m]
I : unit tensor [-]
n : unit vector [-]
P : gas pressure [Pa]
P_s : solid pressure [Pa]
Re_k : Reynolds number [-]
t : time [s]
v : velocity [m/s]
v′ : fluctuating velocity [m/s]
x : radial distance from center of the riser [m]
y : radial distance from center of the riser [m]
z : axial distance from bottom of the riser [m]

Greek Letters

β_{gs} : gas-particle interphase drag coefficient [kg/s m^3]
ε : volume fraction [-]
$\varepsilon_{s,max}$: solid volume fraction at maximum packing [-]
ϕ : specularity coefficient [-]
ϕ_s : exchange of fluctuating energy between gas and solid [kg/m s^3]
γ_s : collisional dissipation of solid fluctuating energy [kg/m s^3]
κ_s : conductivity of the fluctuating energy [kg/m s]
μ : viscosity [kg/m s]
θ : classical granular temperature [m^2/s^2]
θ_t : turbulent granular temperature [m^2/s^2]
ρ : density [kg/m^3]
τ : stress tensor [Pa]
ξ : bulk viscosity [kg/m s]

Subscripts

g : gas phase
s : solid phase
x : radial direction
y : radial direction
z : axial direction

REFERENCES

1. D. Kunii and O. Levenspiel, *Fluidization engineering*, Butterworth-Heinemann, New York (1991).
2. J. R. Grace, A. A. Avidan and T. M. Knowlton, *Circulating fluidized beds*, Blackie Academic & Professional, London (1997).
3. D. Geldart, *Powder Technol.*, **7**, 285 (1973).
4. P. Lettieri, G. Saccone and L. Cammarata, *Chem. Eng. Res. Des.*, **82**, 939 (2004).
5. J. Baeyens and D. Geldart, *Chem. Eng. Sci.*, **29**, 255 (1974).
6. C. G. J. Baker and D. Geldart, *Powder Technol.*, **19**, 177 (1978).
7. L. De Luca, R. Di Felice, P. U. Foscolo and P. P. Boattini, *Powder Technol.*, **69**, 171 (1992).
8. D. Gidaspow, *Multiphase flow and fluidization: Continuum and kinetic theory description*, Academic Press, Boston (1994).
9. Fluent Inc., *Fluent 6.2.16 User's Guide*, Fluent Inc., Lebanon (2003).
10. L. C. Gomez and F. E. Milioli, *Powder Technol.*, **132**, 216 (2003).
11. M. L. Mastellone and U. Arena, *Chem. Eng. Sci.*, **54**, 5383 (1999).
12. P. D. Noymer, M. R. Hyre and L. R. Glicksman, *Int. J. Heat Mass Transfer*, **43**, 3641 (2000).
13. X. Wang, B. Jin and W. Zhong, *Chem. Eng. Process.*, **48**, 695 (2009).
14. J. D. Wilde, G. B. Marin and G. J. Heynderickx, *Chem. Eng. Sci.*, **58**, 877 (2003).
15. P. C. Johnson and R. Jackson, *J. Fluid Mech.*, **176**, 67 (1987).
16. E. Cruz, F. R. Steward and T. Pugsley, *Powder Technol.*, **169**, 115 (2006).
17. B. Chalermsinsuwan, P. Kuchonthara and P. Piumsomboon, *Chem.*

Eng. Process., **48**, 165 (2009).
18. B. Chalermsinsuwan, P. Piumsomboon and D. Gidaspow, *Chem. Eng. Sci.*, **64**, 1195 (2009).
19. R. Clift and J. R. Grace, in *Fluidization II*, J. F. Davidson, R. Clift and D. Harrison Eds., Academic Press, London (1985).
20. S. H. Lee, D. H. Lee and S. D. Kim, *Korean J. Chem. Eng.*, **19**(2), 351 (2002).